PERGAMON

Acta mater. Vol. 47, Nos 15/16, pp. 3939–3951, 1999
© 1999 Acta Metallurgica Inc.
Published by Elsevier Science Ltd. All rights reserved.
Printed in Great Britain
1359-6454/99 $20.00 + 0.00

PII: S1359-6454(99)00255-4

ATOMIC-SCALE STRUCTURE AND CHEMISTRY OF CERAMIC/METAL INTERFACES—I. ATOMIC STRUCTURE OF {222} MgO/Cu (Ag) INTERFACES

D. A. SHASHKOV[1], **M. F. CHISHOLM**[2] **and D. N. SEIDMAN**[1]†

[1]Department of Materials Science and Engineering, Northwestern University, Evanston, IL 60208-3108, U.S.A. and [2]Solid State Division, Oak Ridge National Laboratory, Oak Ridge, TN 37831-6030, U.S.A.

Abstract—Ceramic/metal (C/M) {222} MgO/Cu (Ag) heterophase interfaces, prepared by internal oxidation, are studied by scanning transmission electron microscopy (STEM). The observed spacing between misfit dislocations (1.45 nm) in a ⟨110⟩ projection is in agreement with the prediction of Bollmann's geometric O-lattice theory and experimental values in the literature for {222} MgO/Cu interfaces. It is concluded that the {222} MgO/Cu (Ag) interfaces are semicoherent and contain a trigonal network of pure edge misfit dislocations parallel to ⟨110⟩-type directions, with an $(a/6)\langle 211\rangle$-type Burgers vector. Misfit dislocations are also found in a standoff position at a distance of a single (111) spacing of the Cu (Ag) matrix. Extra intensity at the interface, in some angular dark-field images indicates silver segregation, in agreement with our atom-probe field-ion microscope results. On the metal side of the interface, extra intensity is observed in five atomic layers, which corresponds to a total silver enrichment of approximately 0.7 *effective* monolayers. © *1999 Acta Metallurgica Inc. Published by Elsevier Science Ltd. All rights reserved.*

Keywords: Scanning transmission electron microscopy (STEM); Binary oxide; Segregation; Dislocations; {222} MgO/Cu (Ag) interfaces

1. INTRODUCTION

Materials containing ceramic and metal phases play a significant role in modern materials technology. Examples include dispersion-hardened alloys, metal-matrix fiber-reinforced composite materials, metal–ceramic welding, oxide films and coatings on the surface of high-temperature alloys, and microelectronic packaging. Ceramic/metal (C/M) interfaces often determine macroscopic mechanical, physical, and chemical properties of these materials. It is widely recognized that to design and to control macroscopic materials properties successfully, a fundamental understanding of the atomic-scale structure and chemistry of C/M interfaces is necessary. From a scientific standpoint, C/M interfaces represent an extreme example, and the most interesting one, of a boundary between two disparate materials. While the theories of metal and ceramic homophase interfaces (grain boundaries) are fairly well developed, heterophase C/M interfaces are a relatively less well-studied subject. As a result of their critical technological importance and strong fundamental interest, C/M interfaces have received a great deal of attention recently [1–3].

This paper focuses on atomic-scale characterization of the structure and chemistry of model C/M interfaces. We present a novel approach to study solute–atom segregation at atomically clean C/M interfaces by internally oxidizing ternary metallic alloys, under conditions where only one of the two solute species is oxidized; thereby producing an atomically clean metal-phase embedded in a metallic matrix. The second unoxidized solute species must redistribute itself between the single-phase solid-solution metallic matrix and the metal-oxide phase to maintain itself in thermodynamic equilibrium in the resulting two-phase system. Equilibrium is achieved by the unoxidized solute species segregating to C/M interfaces. In Part I, the structure of the {222} MgO/Cu (Ag) interface is studied using a dedicated scanning transmission electron microscope (STEM). In Part II, the chemistry of {222} MgO/Cu (Ag) and {222} CdO/Ag (Au) interfaces is determined in a direct, quantitative manner by atom-probe field-ion microscopy (APFIM). These measurements are complemented by subnanometer-resolution electron energy loss spectroscopy (EELS).

Internal oxidation is a simple and effective technique to study C/M interfaces. The advantages of this approach are: (1) clean interfaces with negligible impurity segregation because of the large total interfacial area to volume ratio; (2) common low-index directions often exist between the ceramic and metal phases, with interplanar spacings suitable for high-resolution electron microscopy (HREM) or STEM; and (3) a simple orientation relationship between the two phases is usually observed. Prior HREM work on the atomic structure of the {222}

†To whom all correspondence should be addressed.

MgO/Cu interfaces produced by internal oxidation [4–7] demonstrated that MgO precipitates are octahedral shaped, with faceting on {222}-type planes of the oxide, and have a cube-on-cube orientation relationship with the metal matrix. In all cases, periodic contrast along the interface is observed, leading to the conclusion that this interface is semicoherent, containing geometrically necessary misfit dislocations spaced at approximately 1.6 nm. The dislocation core structure, however, was not resolved due to resolution limitations and geometrical reasons discussed in this paper. The lattice misfit parameter between the two lattices, η, is given by $\eta = 2(a_{\text{oxide}} - a_{\text{metal}})/(a_{\text{oxide}} + a_{\text{metal}})$. The value of η is 0.1512, for the room temperature lattice constants, $a_{\text{MgO}} = 0.4212$ nm and $a_{\text{Cu}} = 0.3620$ nm.

STEM has been widely utilized for characterizing materials. Recent advances in this technique are a result of the introduction of dedicated STEMs equipped with field-emission guns that lead to a great improvement of spatial resolution at the sub-nanometer level [8, 9]. As a result, a dedicated STEM provides a powerful tool for acquiring atomic-resolution images of crystalline materials, combined with compositional sensitivity by means of Z-contrast imaging. A major advantage of STEM over HREM is the nearly intuitive interpretability of the annular dark field (ADF) STEM images. Image and contrast formation in the ADF detector is critically dependent on the inner collection angle of the ADF detector, as well as on the nature of the specimen. At small collection angles, image formation is equivalent to HREM image formation under hollow-cone illumination conditions. Image resolution, therefore, is also improved with respect to HREM; image formation, however, primarily involves beams from coherent Bragg scattering and contrast is dominated by diffraction and phase effects. These images exhibit high intensity and strong, nonlinear thickness dependence with possible contrast reversal [10]. When the inner detector angle is increased, thermal diffuse scattering (TDS) overtakes coherent Bragg scattering. Analyses of ADF image formation by thermally scattered electrons [10–12] demonstrate that, to a first approximation, the scattered intensity for each atom is proportional to the square of its atomic number (Z). This classical Coulomb limit is obtained by ignoring the screening of the potential of the nucleus by the electron cloud. In practice, the screening effect reduces the Z-dependency of the scattered intensity to Z^n, where $n = 1.6$–1.9, depending on the ADF detector geometry [10]. This Z-dependency provides a basis for the chemical sensitivity of an ADF image.

Despite significant efforts, a complete theoretical description of the mechanism of incoherent ADF image formation has not yet been established. It was shown that the reduction of coherence in the ADF image originates from two factors; finite dimensions of the ADF detector that average out in-phase contributions from coherent elastically scattered electrons [10] and partial destruction of phase relations by TDS. The condition for incoherence arises from the requirement that image formation is dominated by TDS. It dictates a lower limit on Θ_1, the inner collection angle, which in the case of a mean quadratic vibration amplitude of 0.03 Å^2 and a 100 kV accelerating voltage, implies that $\Theta \geq 90$ mrad. This condition imposes a strict limitation on the ADF detector geometry; increasing Θ_1 to 100 mrad or higher causes an unacceptably low image intensity [13]. An alternative approach involves using an intermediate inner detector angle of 30–50 mrad. At these angles, however, there is a coherent contribution to the image. It was shown by image simulation [14] that if a crystal is oriented along a low-index zone axis, only limited intra-column coherence is preserved, while inter-column interference becomes negligible. Thus, an entire column of atoms acts as a single scattering center. This implies that a high-angle ADF (HAADF) image is a convolution of the incident probe intensity, rather than electron wavefunction, with a specimen object function.

If a specimen is oriented along a particular zone axis, channeling of the electron beam parallel to the atomic columns leads to preservation of its shape. As a result, for sufficiently thin specimens, the spatial resolution of the collected signal is maintained throughout the specimen and ultimately approaches the incident probe diameter. Since channeling conditions are easily destroyed, ADF images are extremely sensitive to such factors as exact crystal orientation, surface contamination, and electron beam damage. The orientation sensitivity of ADF images is stronger than that of conventional HREM images and requires precise positioning of a specimen. It also, however, gives rise to a strong sensitivity of the contrast due to local atomic displacements, caused by atomic imperfections such as misfitting dopant atoms or dislocations [15]. Short- and long-range elastic strain fields may complicate ADF images of imperfections. In addition, while the channeling effect provides conditions for atomic-resolution imaging, it also introduces thickness effects in the zone axis images [16]. This situation is further complicated by the fact that electrons channel for considerably different distances along atomic columns of different atomic numbers. In combination with the experimental complications considered in this paper, it makes the ADF STEM analysis of heterophase interfaces a challenging problem. To the best of our knowledge, this study represents a first attempt to determine the atomic structure of C/M heterophase interface by HAADF imaging. We report the observation of misfit dislocations at the {222} MgO/Cu (Ag) interface. Images are then analyzed to determine the dislocation structure of this heterophase interface.

Some of the dislocations are found in a standoff position. Experimental data on the standoff effect are reviewed and compared with the available theory. Silver segregation at this interface is detected in the HAADF images, which is consistent with our APFIM results presented in Part II. Experimental challenges associated with analysis of C/M heterophase interfaces are discussed.

2. EXPERIMENTAL PROCEDURE

The alloy for this study, with the nominal composition Cu–2.5 at.% Mg–0.8 at.% Ag, was prepared from elements with high initial purity by arc melting in pure argon gas. C/M heterophase interfaces were produced by internal oxidation of thin sheets (150–200 μm thick) employing the Rhinespack technique [17] in a 1:1:1 (vol.) mixture of Cu, Cu_2O and Al_2O_3 powders at 950°C for 2 h. These experimental conditions yield an oxygen partial pressure of 10^{-2} Pa. To maximize the level of Ag segregation at {222} MgO/Cu heterophase interfaces, the specimens were subsequently annealed in argon at 500°C for 6 h. This time was chosen on the basis of the known bulk diffusivity of Ag in Cu [18–20] (the activation energy and the pre-exponential factor are, respectively, 194.7 kJ/mol and 0.61 m^2/s) and the average distance between MgO precipitates of ≈46 nm; the latter was measured by TEM. Specimens were electropolished to produce electron-transparent thin areas and then ion milled for 10 min at room temperature, immediately prior to STEM observations, to reduce surface contamination levels. Silver segregation levels at the {222} MgO/Cu (Ag) interface were quantitatively measured by APFIM and confirmed by EELS, as described in Part II. It is found that an average segregation level of silver at this heterophase interface corresponds to 0.2 *effective* monolayers. The key steps in the experimental procedure are schematically summarized in Fig. 1.

For the STEM studies, a VG HB603 300 kV microscope at Oak Ridge National Laboratory was utilized. It is equipped with a cold field-emission gun with a 0.3 eV energy spread and its objective lens has a 1.0 mm coefficient of spherical aberration. The incoherent resolution of this instrument is 0.13 nm [21]. The ultrahigh vacuum in the column of this STEM is about 5×10^{-8} Pa, allowing for very low surface contamination levels. Prior to high-resolution imaging, the areas of interest in the samples were flood electron-illuminated for 20 min, to reduce the buildup of hydrocarbon contamination when employing a highly focused electron beam; this treatment does not produce radiation damage at the C/M interface. An inner collector angle of the ADF detector of 45 mrad was utilized. It was shown that under this condition, the contribution of strain contrast to the image is negligible [22]. Grayscale images (480 × 480 pixels) were digitally recorded with a typical acquisition time of 17 s per frame. All images presented in this paper are raw, unfiltered images with the dynamic range expanded for publication purposes.

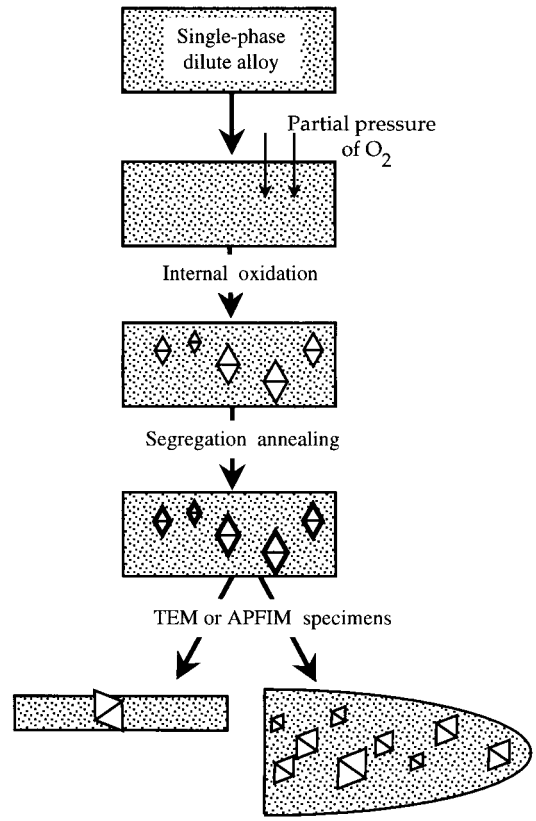

Fig. 1. Schematic diagram illustrating the key steps required to produce and study solute segregation at ceramic/metal interfaces.

3. RESULTS

3.1. Conventional transmission electron microscopy

TEM observations demonstrated that the MgO/Cu (Ag) specimens contain MgO precipitates, which are morphologically identical to the ones found in the undoped MgO/Cu system [4–7]; that is, the MgO precipitates, 10–50 nm in diameter, have a cube-on-cube orientation relationship with the Cu (Ag) matrix and are octahedral-shaped with faceting on {222} planes. Here and later, the diameter of a precipitate is defined as the distance between two of its opposite parallel {222} facets. Therefore, for an octahedral precipitate, the diameter d is related to its edge length, L, by $d = 2L/\sqrt{6}$. No phases other than the solid-solution Cu (Ag) matrix and MgO were detected. Figure 2 is a bright-field TEM micrograph of an internally oxidized MgO/Cu (Ag) specimen exhibiting a high number density ($\approx 1.0 \times 10^{22}/m^3$) of MgO precipitates with a mean diameter of about 20 nm. Shown in the inset is a selected area diffraction pattern recorded for a 110-

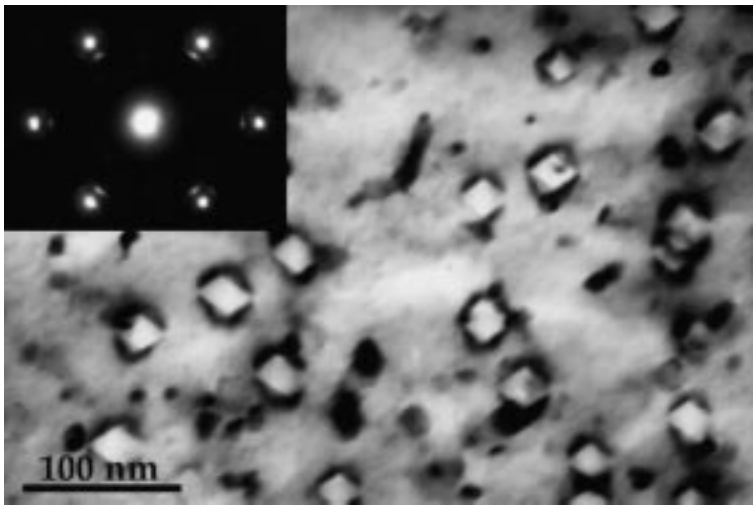

Fig. 2. Multi-beam bright-field TEM micrograph of an internally oxidized MgO/Cu (Ag) specimen; inset, (110) selected area diffraction pattern exhibiting satellite reflections associated with the main reflections from Cu (Ag) matrix.

zone axis. In addition to the primary reflections from the Cu (Ag) matrix, satellite diffraction spots are visible that correspond to MgO in the cube-on-cube orientation.

3.2. Interface morphology

While microscopically facets of the MgO precipitates appear flat, to first order, it was found that in many cases the {222} interfaces contain double or quadruple-height atomic steps. Interfacial steps near the corners of the particles have previously been found for the MgO/Cu system by HREM [6]. Figure 3 is a [110] image of a {222} interface with both double- and quadruple-height atomic steps. We define the single-height step as $d_{\{222\}}(\mathrm{MgO}) = 0.122$ nm, while a double-height step is $2d_{\{222\}}(\mathrm{MgO}) = 0.243$ nm. In MgO, the {222} planes are polar, consisting of either oxygen or magnesium ions. Consequently, two possible terminations of a polar ceramic/metal interface are possible—anion or cation. The steps in Fig. 3 have heights of $2d_{\{222\}}(\mathrm{MgO}) = 0.243$ nm and $4d_{\{222\}}(\mathrm{MgO}) = 0.486$ nm. Therefore, they do not change the chemical composition of the terminating plane—oxygen ion [7].

3.3. Dislocation structures of {222} MgO/Cu (Ag) interfaces

Due to the two-dimensional projective character of the STEM technique, the observed dislocation structure of an interface depends on the specimen orientation. For a {222} interface, the two main possibilities for STEM observations are the ⟨110⟩ and ⟨211⟩ orientations. The ⟨211⟩ projection is rarely used as the resolving power of most microscopes is insufficient to image Cu {220} fringes spaced at 0.128 nm. In this work, while it was possible to obtain clearly resolved Cu {220} in the bulk and Mg {220} fringes in the MgO precipitates, the atomic structures of interfaces were not resolved for a ⟨211⟩-type projection.† Therefore, a ⟨110⟩-type projection was used to determine the interfacial dislocation structure. Figure 4 exhibits bright-field (BF) and HAADF images of a {222} MgO/Cu (Ag) heterophase interface in a ⟨110⟩ orientation. Local bending of the atomic planes is clearly visible and arrows indicate the positions of regions of "bad" fit. The average spacing between these dislocations is 1.45 ± 0.19 nm, where 0.19 nm is one standard deviation and the average value 1.45 nm is for 20 dislocations.

In addition to regular misfit dislocations, a partial misfit dislocation was found at the corner of a precipitate, see Fig. 5(a). A Shockley partial dislocation with an $(a/6)\langle 211\rangle$-type Burgers vector is observed at the junction of two facets. Extending along a {111} plane of the Cu (Ag) matrix is a stacking fault terminated by another $(a/6)\langle 211\rangle$ Shockley partial dislocation at a distance of about 1.5 nm. Figure 5(b) details the atomic layer sequence associated with this planar imperfection. As noted in Ref. [6], this type of imperfection accommodates a rigid-body translation between two equivalent interface structures present on adjacent {222} facets.

Finally, most of the misfit dislocations observed in the {222} MgO/Cu (Ag) system terminate at the interface, without any apparent shift of the dislo-

†In recent research, to appear in *Phil. Mag. A* (1999), Groen *et al.* studied the MgO/Cu interface for a ⟨211⟩-type projection employing the atomic-resolution microscope (ARM) 1250 at the Max-Planck Institut, Stuttgart, which has a point-to-point resolution of 0.12 nm. They conclude, "the increased resolution of the ARM, compared to the 4000EX, does not lead to more clearly resolved strain fields of the misfit dislocations".

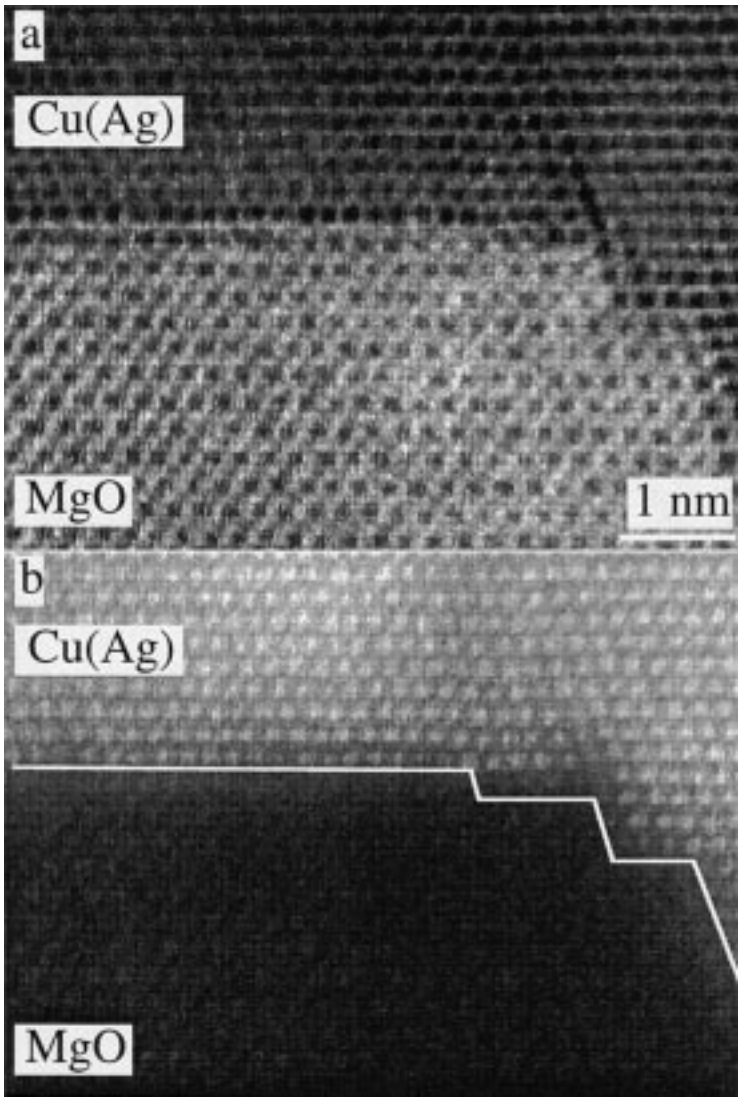

Fig. 3. (a) BF and (b) HAADF images of a {222} MgO/Cu (Ag) heterophase interface recorded along the common [110] direction. Both double- and quadruple-height atomic steps are seen near the corner of this MgO precipitate. A white line indicates the position of the interface.

cation core into the metal matrix; the latter is the so-called standoff dislocation effect [23]. Some sections, however, of the C/M interfaces are found to have a terminating Cu (Ag) layer stretched along the interface to match the lattice parameter of MgO, with the core of the dislocation residing in the second Cu (Ag) layer. An atomically flat interface is shown in Fig. 6(a). Figure 6(b) is a schematic diagram of this interface structure with one misfit dislocation in a standoff position. Its standoff distance is equal to a single {111} spacing of the Cu (Ag) matrix (0.208 nm).

3.4. Evidence of silver segregation at a {222} MgO/Cu (Ag) interface

Figure 7 is an HAADF image of a {222} MgO/Cu (Ag) interface imaged in a ⟨110⟩ orientation. In this case, matrix atoms cover the precipitate, so the heavier Cu (Ag) matrix dominates the observed lattice spacing. A bright halo is visible on the metal side of this interface. An intensity line scan demonstrates a 32% increase in intensity for the first two {111} planes, while the region of extra intensity is spread over five {111} planes in the Cu (Ag) matrix. This effect is due to silver segregation at this interface. This result is discussed in Section 4.4.

4. DISCUSSION

4.1. Atomic and dislocation structure of {222} interface

According to Bollmann's geometric O-lattice theory, the dislocation structure of a semicoherent {111} interface between two cubic lattices must be a hexagonal net of pure edge dislocations; the dislocation line segments must be parallel to the ⟨211⟩

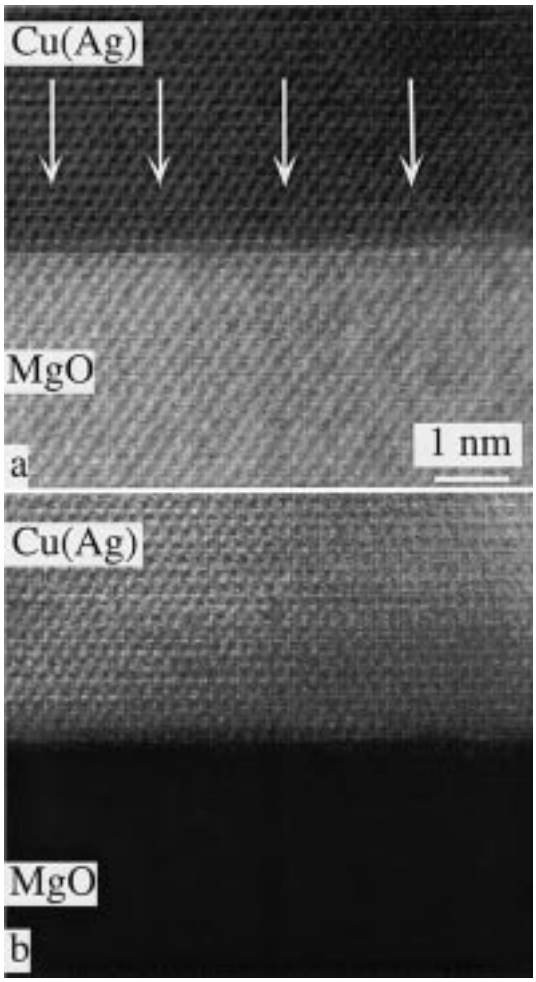

Fig. 4. (a) BF and (b) HAADF images of a {222} MgO/Cu (Ag) heterophase interface recorded along the common [110] direction. Arrows indicate the positions of misfit dislocations. The average spacing between dislocations is 1.45 $\pm$0.19 nm.

directions with a Burgers vector of $(a/2)\langle 110\rangle$ [24]. Figure 8(a) exhibits a hexagonal misfit dislocation pattern on a {222} facet of an octahedral precipitate. The size of an hexagonal cell is determined by the lattice misfit parameter, η, which is 15.1% for the MgO/Cu system. This corresponds to the distance between two parallel sides of a hexagon of 1.81 nm, see Fig. 8(b). In the [112] projection, see Fig. 8(c), some segments of this dislocation structure are projected end-on, giving an opportunity to determine the structure of dislocation cores, if an HREM or a STEM can resolve the 0.128 nm spacing of {220} lattice fringes in copper. The continuous segments are, however, only 1 nm in length for the {222} MgO/Cu system due to the high lattice misfit. Therefore, direct imaging of dislocation cores does not seem possible in this case, as a specimen thickness of 1 nm or less would not produce a reasonable image in either an HREM or a STEM.

Alternatively, in a [110] orientation, the dislocation structure shown in Fig. 8(a) is more favorable for imaging. A projected image represents regions of good fit, separated by the regions of "bad" fit [see Fig. 8(d)]. Regions of good fit are about 1 nm wide and only contain dislocation lines lying in the plane of the image. Their Burgers vectors are parallel to the electron beam, so the local atomic displacements caused by these dislocations do not, to a first approximation, disturb the registry between the projected Cu and MgO planes. Regions of good fit are separated by a zigzag dislocation pattern with a projected width of 0.5 nm. Dislocations in this pattern are inclined 30° with respect to the electron beam, so their core structure cannot be resolved.

The predictions of O-lattice theory are in qualitative agreement with the observed periodicity at the interface. Quantitatively, the measured spacing (1.45 nm) is smaller than the theoretically predicted spacing of 1.54 nm by 6%. The main discrepancy, however, between the predicted and observed dislocation structures, is the clear visibility of the atomic columns along the interface, including the regions of "bad" fit (see Figs 3–6). This is only possible in two cases: if the interface is incoherent or if the misfit dislocation lines are end-on. The {222} MgO/Cu interfaces observed in this work are obviously not incoherent. First, a Burgers circuit around any misfit dislocation shown in Fig. 7 does not close. Secondly, a local displacement field is clearly visible near the interface. Therefore, we conclude that these heterophase interfaces are semicoherent.

An alternative model of a {111} interface between two cubic lattices has been proposed in the literature and experimentally observed at {111} GeSi/Si interfaces [25, 26]. It consists of a trigonal network of straight edge dislocations having a $\langle 110\rangle$-type line direction and a Burgers vector of the type $(a/6)\langle 211\rangle$, see Fig. 8(e). As shown in Fig. 8(f), this structure can be obtained by dissociation of the triple nodes of the original hexagonal net into interfacial stacking faults (SFs), bounded by triangles of $(a/6)\langle 211\rangle$ dislocations. An analogous dislocation network was observed in simulations of {222} MgO/Cu interfaces [27–29] based on *ad hoc* interatomic potentials designed to have the correct periodicity of {222} MgO/Cu interfaces, but otherwise not based on a detailed model of interfacial bonding. Recently, this trigonal network was obtained at {222} MgO/Cu interfaces from molecular dynamics (MD) simulations based on interatomic potentials derived from first principle LDFT calculations [30–33]. Calculations of the relaxed structures for both dislocation configurations [27–29] demonstrated that the trigonal structure has a much smaller strain field compared to the hexagonal structure. Therefore, the trigonal structure may be energetically favorable for systems in which the gain in the elastic energy is greater than the energy of the created interfacial stacking faults. This argument is applicable to the {222} MgO/Cu (Ag) inter-

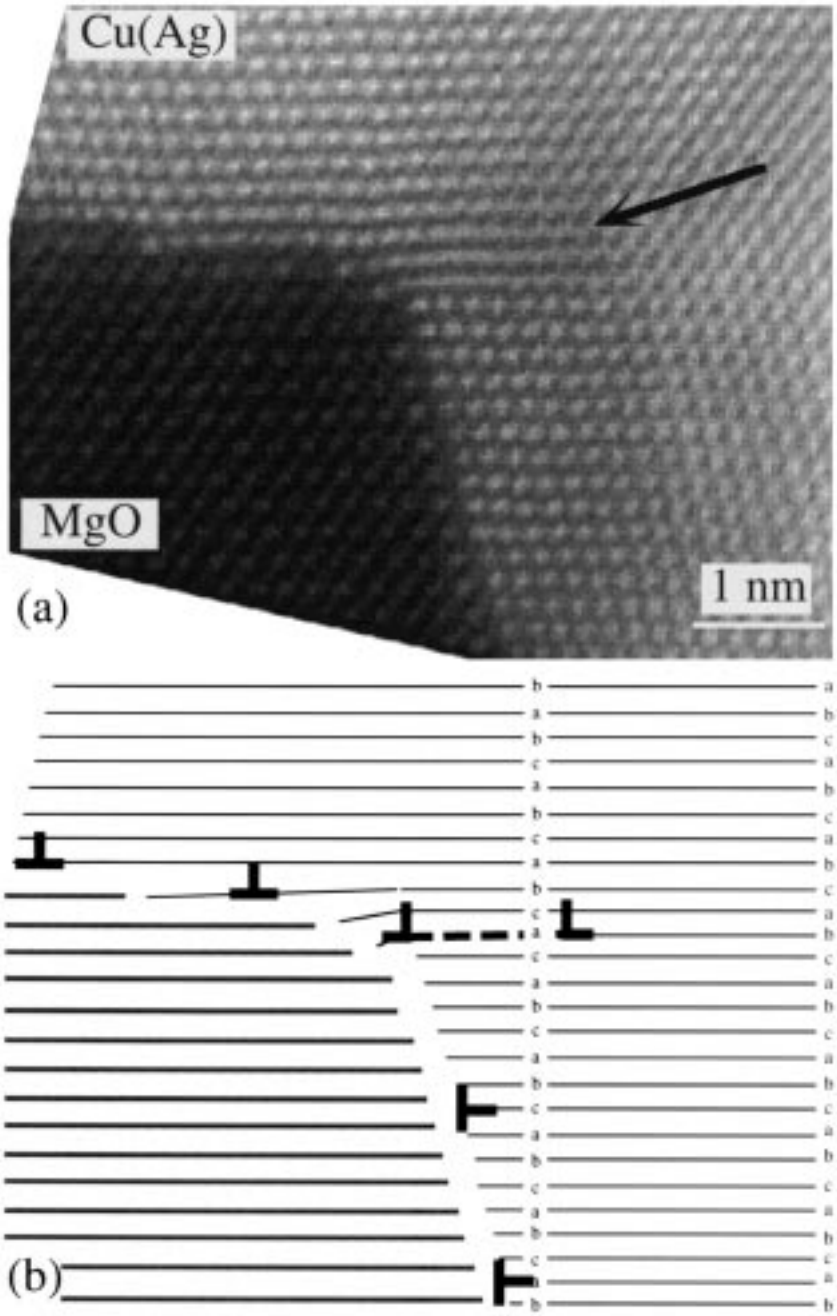

Fig. 5. (a) An HAADF image of the corner of a MgO precipitate in a Cu (Ag) matrix. Double-height steps are visible near the intersection of two {222}-type facets. Note the contrast disturbance near the corner indicated by an arrow. (b) A schematic diagram of the image in (a) showing the {222} planes of MgO and Cu (Ag) and the positions of misfit dislocations. The contrast disturbance in (a) is due to a Shockley partial dislocation at the interface with a Burgers vector $(a/6)\langle 211\rangle$. A stacking fault is emitted into the matrix and is terminated by another Shockley partial. The stacking sequence in the matrix is indicated schematically in (b).

face since its energy is decreased by the presence of silver at the interface, that is, Gibbsian interfacial segregation. In MD simulations [30–33], it was found that the trigonal dislocation network is the lowest energy structure for the {222} MgO/Cu interface at 0 K. The MD simulations, based on classical potentials has the following limitations: (1) the potential is based on first principle calculations for coherent interfaces and the influence of this misfit is neglected; (2) only one parallel translation in the initial configuration was employed, so the final relaxed configuration may be biased. First principles calculations in progress on cells, containing upwards of 399 atoms, that allow for relaxations of

both the Cu and MgO lattices, should be capable of definitively allowing for a comparison of the energies of the hexagonal and trigonal interfacial dislocation networks.

In principle, the trigonal and hexagonal networks are distinguishable by HREM [27–29], but it has proven difficult, so far, to make a definitive identification on the basis of experiment alone. Clear visibility of the atomic columns along the interface in this study, including the regions of "bad" fit, indicates that the dislocation lines are parallel to the beam direction, ⟨110⟩. Taking into account the MD simulation results [30–33], subject to the above stated caveats, it is concluded that the {222} MgO/Cu (Ag) interfaces are semicoherent and contain a trigonal network of pure edge misfit dislocations. Dislocation lines are parallel to the ⟨110⟩-type direction and have $(a/6)\langle 211\rangle$-type Burgers vectors.

4.2. Interfacial standoff dislocations at {222} interface

The standoff effect has been observed in a variety of C/M systems. There have been several attempts to explain this effect and to predict an equilibrium standoff distance. A theory based on isotropic elasticity of the standoff effect [23] suggests that the driving force for the standoff effect is the difference in elastic moduli between the ceramic and metal phases. It is energetically favorable to shift dislocation cores into the metal to minimize the elastic strain energy in the stiffer ceramic phase. An equilibrium standoff distance is then determined by the balance between an image force that repels a dislocation away from an interface to lower the elastic strain energy in the ceramic, and an attractive coherency force that reflects an energetic advantage

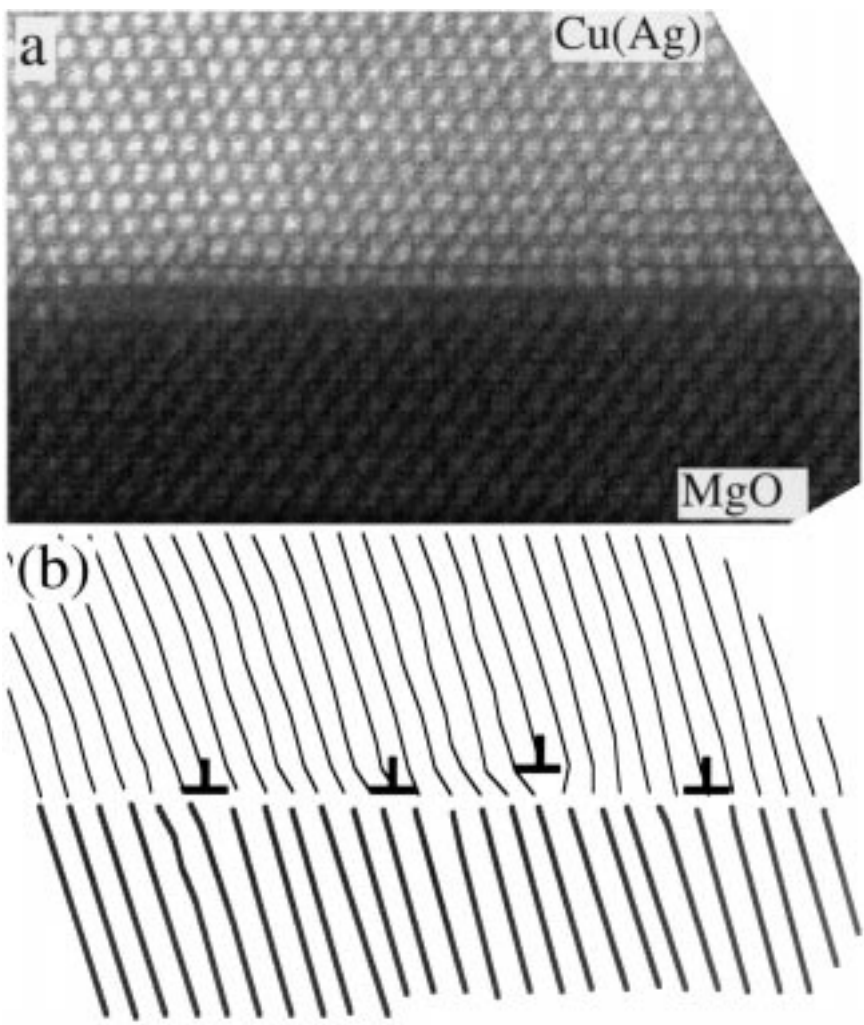

Fig. 6. (a) An atomically flat {222} MgO/Cu (Ag) interface in a ⟨110⟩-type projection. (b) Schematic diagram of the misfit dislocation structure for the interface shown in (a). Note that one of the dislocations is in a standoff position.

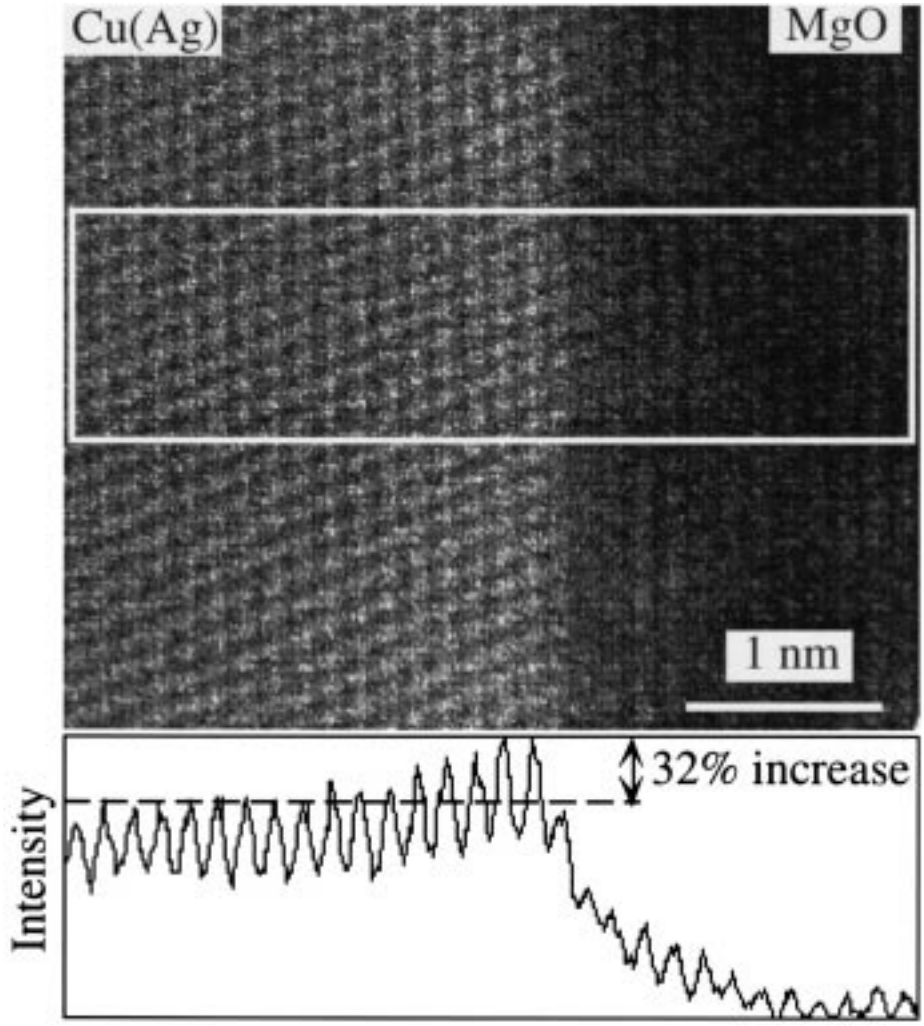

Fig. 7. An HAADF image (inner detector angle 45 mrad) of a {222} MgO/Cu (Ag) interface recorded along the common [110] direction. An intensity linescan taken from the rectangular area exhibits a 32% increase in brightness in the first and second Cu (Ag) {111} planes. Extra intensity is, however, visible in five {111} planes in the Cu (Ag) matrix. This indicates the presence of silver segregated at this interface.

of a semicoherent interface over a fully coherent one. Based on these assumptions, an equilibrium standoff distance (D_{standoff}) was derived using linear isotropic elasticity theory [23]:

$$D_{\text{standoff}} = -\frac{A+B}{8\pi(\alpha+1)}\frac{b_{\text{i}}}{\eta} \tag{1}$$

where b_{i} is the in-plane component of a Burgers vector; η is the fractional lattice misfit parameter defined in Section 1, and A, B, and α are constant expressions containing the elastic constants, which are a measure of the elastic mismatch between the two materials. An important consequence of equation (1) is that the standoff distance is inversely proportional to η. Therefore, it is expected that C/M systems with a strong elastic mismatch and a small value of the lattice misfit parameter, η, will have the largest values of D_{standoff}. The experimental values of D_{standoff} observed in different C/M systems are summarized in Table 1. To test the correlation predicted by equation (1), Fig. 9 exhibits a plot of the standoff distances in C/M systems vs $1/\eta$. An analysis of the data presented in Table 1 allows the following observations:

1. Equation (1) predicts only the general trend. Prior to our research, no standoff effect has been observed for any system with $\eta > 0.1$. Calculated values, however, seem to underestimate the observed standoff distances.
2. For a single C/M system, the standoff effect may vary dramatically. For the (0001)Al_2O_3/Nb system, for example, the reported standoff distance varies from 0 to 1.2 nm, depending on the method of interface fabrication. Factors such as processing conditions, oxygen partial pressure, and the presence of imperfections and impurities

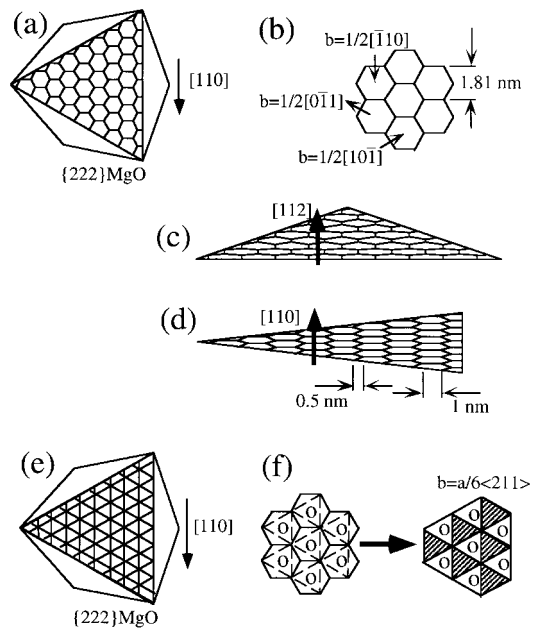

Fig. 8. Dislocation structures at a {222} MgO/Cu (Ag) interface. (a) Misfit dislocation pattern on a {222} facet of an octahedral precipitate, according to O-lattice theory. (b) Dimensions and Burgers vectors of misfit dislocation pattern in (a) for a {222} MgO/Cu interface. (c) {222} facet of an octahedral MgO precipitate in (a) compressed along a [112] direction. Dislocation-free regions separate end-on dislocation segments. (d) {222} facet of an octahedral MgO precipitate in (a) compressed along a [110] direction. Regions of good fit are 1 nm wide. Regions of "bad" fit are 0.5 nm wide and contain a 30° zigzag dislocation pattern. (e) An alternative model of the dislocation structure for the {222} interface with trigonal symmetry. (f) A schematic diagram showing decomposition of the dislocation structure in (a). The resulting dislocation structure has trigonal symmetry and consists of straight edge dislocations. Triangular areas at the interface are alternating regions of good fit (indicated by "O" symbols) and interfacial stacking faults (shaded areas).

can affect the kinetics of misfit dislocation nucleation, mobility, and the resulting interface structure.

Standoff dislocations have not heretofore been observed at {222} MgO/Cu interfaces. According to equation (1), the equilibrium standoff distance at the {222} MgO/Cu interface should be 0.02 nm [6]. As suggested in Ref. [3], equation (1) is derived based on linear elasticity theory and may, therefore, underestimate the energy of misfit dislocation cores. In addition, the presence of 13 at.% oversized silver atoms, with respect to copper, at the interface may affect the equilibrium standoff distance. Since only a few of the observed {222} MgO/Cu (Ag) interfaces contain standoff dislocations at a single {111} spacing, it is suggested that the "normal" configuration is slightly energetically preferred over the standoff configuration for this system.

4.3. Interfacial steps at {222} interface

It is also noteworthy that all the steps observed in the {222} MgO/Cu (Ag) system are either double or quadruple the $\{222\}_{MgO}$ height. This implies that a single type of ion termination of these polar {222} interfaces is always maintained, oxygen ion [41–43]. Otherwise, the interface separation on both sides of a step would differ. Since oxygen layers are invisible in STEM, the observed structure may or may not incorporate an oxygen layer between the last Mg layer of MgO and the terminating {111} plane of Cu. It has, however, been established experimentally by APFIM that the oxygen termination at atomically clean {222} MgO/Cu interfaces is at least strongly preferred [41–43]. Results of first principle LDFT calculations of atomically clean {222} MgO/Cu interfaces, in the zero-misfit approximation [44], also indicate that oxygen and magnesium terminations produce far different adhesive energies, 2.9 and 1.7 eV/atom, thus further substantiating this point. Finally, our high-resolution EELS analyses of {222} MgO/Cu interfaces [45] has also demonstrated that this interface is oxygen terminated. Thus, we conclude that the {222} MgO/Cu (Ag) interfaces of this study are also oxygen terminated from three different experimental techniques, and lastly the LDFT calculations [44] agree with those experiments.

Table 1. Standoff distance ($D_{standoff}$) for ceramic/metal systems

Interface	Fabrication method[a]	η	$D_{standoff}$ (nm)	Ref.
{222} MgO/Cu	IO	0.153	0	[4–6]
{222} CdO/Ag	IO	0.136	0	[34]
{222} MgO/Nb	MBE	0.104	0	[35]
{100} MgO/Nb	MBE	0.098	0.47–0.93	[35]
{222} MgO/Pd	IO	0.076	0–0.22	[4, 5]
{222} MgO/Pd	IO	0.076	0.39–0.78	[6]
{222} MnO/Cu	IO	0.064	0.42	[36]
{100} NiO/Pt	DB	0.061	0.59–0.78	[24]
(0001) Al_2O_3/Nb	MBE	0.055	1.2	[35]
{01$\bar{1}$2} Al_2O_3/Nb	IO	0.032	0.93	[37]
{100} MgO/Ag	MBE	0.032	0	[38]
{222} NiO/Ag	EO	0.022	0.47–0.71	[39]
(0001) Al_2O_3/Nb	MBE	0.019	0	[40]

[a] IO, internal oxidation; MBE, molecular beam epitaxy; DB, diffusion bonding; EO, external oxidation.

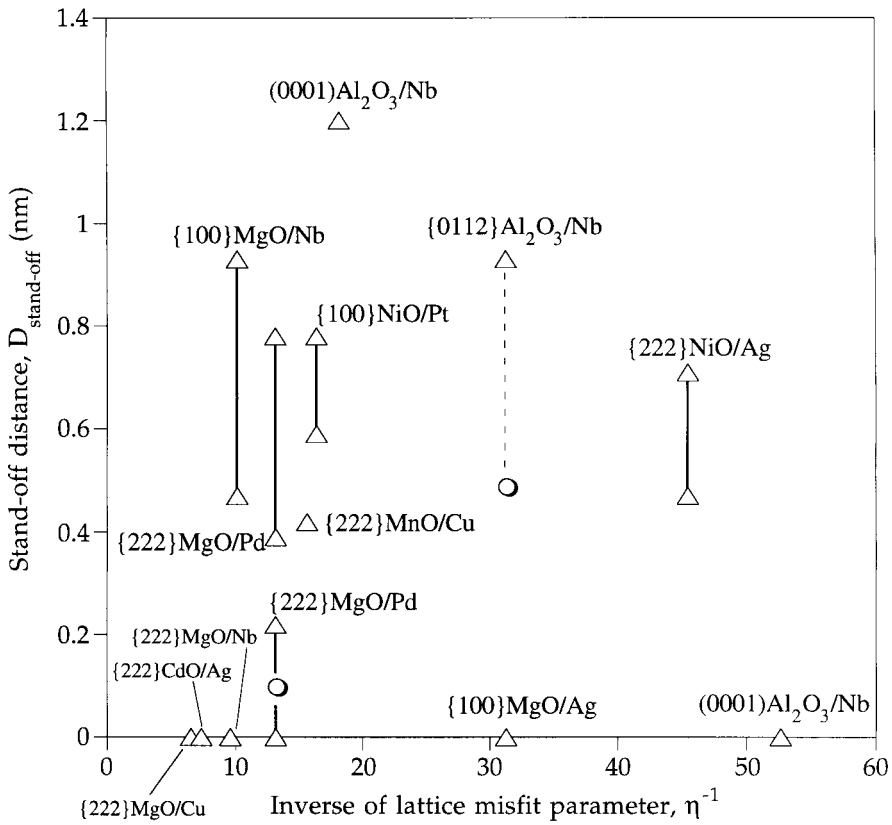

Fig. 9. Standoff distance, $D_{standoff}$, in ceramic/metal systems vs inverse of lattice misfit parameter, η. Open triangles are for experimental data, while the open circles are predictions calculated from equation (1). References to the experimental data are listed in Table 1.

4.4. Interfacial segregation of silver at {222} interface

As discussed in Section 1, the chemical sensitivity of Z-contrast is Z^n, where $n = 1.6$–1.9, depending on the ADF detector geometry—it is Z^2 in the ideal (unscreened) case. The ratio of the squares of atomic numbers is 2.63 for the Ag–Cu pair and 15.34 for the Ag–Mg pair. Calculations predict [10] that for the value of the inner detector angle of 45 mrad used in this work; the parameter n is equal to approximately 1.65. Taking the worst case scenario ($n = 1.6$), the Z-ratio becomes 2.17 for the Ag–Cu pair and 8.89 for the Ag–Mg pair. This makes the MgO/Cu (Ag) system favorable for detecting the presence of silver at an interface by Z-contrast. All the HAADF images, however, shown in Figs 3–6, do not exhibit this extra intensity in the vicinity of the interface. All interfaces in Figs 3–6 represent *uncovered* precipitates; that is, they go through the entire thickness of the specimen, so there is no matrix contribution to the volume of the precipitate. While this configuration is essential for imaging the interface structure, it did not allow us to detect silver segregation at the interface by Z-contrast. Figure 7, however, is a HAADF image of a {222} MgO/Cu (Ag) interface that exhibits extra intensity, which is due to silver segregation.

The investigation of interfacial segregation by atomic-resolution Z-contrast microscopy is a relatively new subject. There have been successful examples [46, 47] of detecting segregation of solute atoms at well-defined, planar homophase interfaces (Ni and B in Ni_3Al grain boundaries). The application of Z-contrast to heterophase interfaces between metal matrix and small oxide precipitates has not heretofore been made. There is no theory at hand describing the effect of elastic strains on image contrast formation. This factor is particularly important for the C/M system studied, because of a 20% mismatch in the thermal expansion coefficients of Cu and MgO (16.5×10^{-6}/K and 13.5×10^{-6}/K, respectively). This effect causes 0.27% elastic strain at the interface over the temperature range 1223–300 K, where 1223 K is the temperature of internal oxidation. As a result, in addition to interfacial strains, thermal mismatch strains are observed around MgO precipitates. The use, however, of a high inner collection angle of the ADF detector (45 mrad) helps to reduce the strain contribution to the contrast to a minimum [22].

There are several geometrical factors complicating an accurate analysis of {222} MgO/Cu (Ag) interfaces. First, due to the triangular shape of a precipitate's {222} facets, there is no region with a constant thickness of MgO along the interface. Another factor contributing to the difficulty of analysis is the presence of interfacial steps. If steps are present parallel to the beam direction, the extra intensity due to segregation is spread over a thicker region and is more difficult to detect. Finally, results of APFIM experiments and atomistic Monte Carlo simulations [48–56] suggest that interfacial segregation need not be limited to a single atomic layer, and that a whole spectrum of segregation sites, with both attractive or repulsive binding energies, may exist at an interface. These sites may be found in several atomic layers parallel to an interface. Therefore, it is reasonable to expect that thermodynamic equilibrium silver segregation, at the {222} MgO/Cu (Ag) interface, is also spread over several atomic planes of copper, making the Z-contrast less distinct.

Despite all of the above factors, the intensity linescan in Fig. 7 exhibits direct evidence for silver segregation. Even though Z-contrast gives only a qualitative picture, the 32% increase in intensity observed in the first two {111} planes of copper allows us to make a rough estimate of the segregation level. If the first two layers contain an amount of silver, X_{Ag}, then we can write for the intensity from each of these layers:

$$X_{Ag} \cdot 2.63 + (1 - X_{Ag}) \cdot 1 = 1.32 \qquad (2)$$

where 2.63 is the square of the ratio of the Z-numbers of Ag and Cu. This yields $X_{Ag} \approx 0.2$ at.fr. in each of the two atomic planes. Summing over five atomic planes exhibiting the extra intensity, we obtain that the total amount of silver at this interface is equal to approximately 0.7 *effective* monolayers (ML); we use the adjective *effective* to emphasize strongly that the segregation is not occurring in a single atomic plane. This estimate is consistent with the levels of silver segregation at these {222} MgO/Cu heterophase interfaces measured by APFIM (0.06–0.44 ML). In Part II, silver segregation at the {222} MgO/Cu (Ag) interface was detected and quantitatively measured by APFIM. The total amount of silver at this interface was found, via APFIM, to be equivalent to approximately 0.2 *effective* monolayers and it is not confined to a single monolayer.

5. CONCLUSIONS

A detailed Z-contrast STEM investigation of solute segregation of Ag at a ceramic/metal interface was performed. It was found that {222} MgO/Cu (Ag) heterophase interfaces are generally flat, with some double- and quadruple-height steps, particularly near the corners of a MgO precipitate.

The dislocation structure of the {222} MgO/Cu (Ag) interface was observed in a ⟨110⟩-type projection. We observed that the regions of "good" and "bad" fit are in agreement with those predicted by Bollmann's geometric O-lattice theory. The observed spacing between dislocations is 1.45 ± 0.19 nm, which is close to other experimental values in the literature for atomically clean {222} MgO/Cu interfaces. The clear visibility of the atomic columns parallel to the interface, including the regions of "bad" fit, indicates that the dislocation lines are parallel to the beam direction, ⟨110⟩-type. Therefore, it is concluded that the {222} MgO/Cu (Ag) heterophase interfaces are semicoherent and contain a trigonal network of edge-character misfit dislocations. The dislocation lines are parallel to the ⟨110⟩-type directions and have $(a/6)\langle 211\rangle$-type Burgers vectors. Several misfit dislocations are found in a standoff position at a distance of a single (111) spacing of the Cu (Ag) matrix (0.208 nm).

Under high-angle ADF imaging conditions, extra intensity is detected at this interface. This indicates silver segregation at this C/M interface, in agreement with our APFIM and EELS experimental results (Part II). On the metal side of the interface, extra intensity is observed in five atomic layers and we estimate that this corresponds to a total silver enrichment of approximately 0.7 *effective* monolayers.

Acknowledgements—Stephen J. Pennycook is thanked for kindly and graciously helping to make this STEM study possible at Oak Ridge National Laboratory and for useful discussions. We kindly thank Roy Benedek for many useful discussions and interactions concerning this study and for serving on the Ph.D. thesis committee of D.A.S. This research was supported by the U.S. Department of Energy at Northwestern University under grant DE-FG02-96ER45597 (D.A.S. and D.N.S.), and at Oak Ridge National Laboratory under contract DE-AC05-84OR21400 (M.F.C.).

REFERENCES

1. Rühle, M., Evans, A. G., Ashby, M. F. and Hirth, J. P. (ed.), *Metal–Ceramic Interfaces: Proceedings of an International Workshop*, Santa Barbara, CA, 16–18 January 1989. Pergamon Press, New York, 1990.
2. Mader, W. and Rühle, M. (ed.), *Proceedings of the International Symposium on Metal–Ceramic Interfaces*, Irsee, Germany. *Acta metall.*, 1992, **40S**.
3. Ernst, F., *Mater. Sci. Engng*, 1995, **R14**, 97.
4. Lu, P. and Cosandey, F., *Ultramicroscopy*, 1992, **40**, 271.
5. Lu, P. and Cosandey, F., *Acta metall.*, 1992, **40S**, 259.
6. Chen, F. R., Chiou, S. K., Chang, L. and Hong, C. S., *Ultramicroscopy*, 1994, **54**, 179.
7. Jang, H., Seidman, D. N. and Merkle, K. L., *Interface Sci.*, 1993, **1**, 61.
8. Crewe, A. V., Langmore, J. P. and Isaacson, M. S., in *Physical Aspects of Electron Microscopy and Microbeam Analysis*, ed. B. M. Siegel and D. R. Beaman. Wiley, New York, 1975, p. 47.

9. Browning, N. D., Chisholm, M. F. and Pennycook, S. J., *Nature*, 1993, **366**, 143.
10. Hartel, P., Rose, H. and Dinges, C., *Ultramicroscopy*, 1996, **63**, 93.
11. Pennycook, S. J. and Jesson, D. E., *Ultramicroscopy*, 1991, **37**, 14.
12. Amali, A. and Rez, P., *Microsc. Microanal.*, 1997, **3**, 28.
13. Pennycook, S. J. and Jesson, D. E., *Acta metall.*, 1992, **40S**, 249.
14. Jesson, D. E. and Pennycook, S. J., *Proc. R. Soc. Lond. A*, 1995, **449**, 273.
15. Perovic, D. D., Rossouw, C. J. and Howie, A., *Ultramicroscopy*, 1993, **52**, 353.
16. Hillyard, S. and Silcox, J., *Ultramicroscopy*, 1993, **52**, 325.
17. Rhines, F. N., Johnson, W. A. and Anderson, W. A., *Trans. Am. Inst. Min. Engrs*, 1942, **147**, 205.
18. Barreau, G., Brunnel, G., Ciceron, G. and Lacombe, P., *C. r. Acad. Sci.*, 1970, **270**, 516.
19. Gorbachev, V. A., Klotsman, S. M., Rabovskiy, Ya. A., Talinsky, V. K. and Timofeyev, A. N., *Fizika Metall. Metalloved.*, 1972, **34**, 879.
20. Gorbachev, V. A., Klotsman, S. M., Rabovskiy, Ya. A., Talinsky, V. K. and Timofeyev, A. N., *Physics Metals Metallogr. (English Trans.)*, 1972, **34**(4), 202.
21. Pennycook, S. J., Jesson, D. E., McGibbon, A. J. and Nellist, P. D., *J. Electron Microsc.*, 1996, **45**, 36.
22. Shashkov, D. A., Ph.D. thesis, Northwestern University, 1997.
23. Mader, W. and Knauss, D., *Acta metall.*, 1992, **40S**, 207.
24. Shieu, F.-S. and Sass, S. L., *Acta metall.*, 1990, **38**, 1653.
25. Ernst, F., *Phil. Mag. A*, 1993, **68**, 1251.
26. Ernst, F., Pirouz, P. and Bauser, E., *Physica status solidi* (a), 1992, **131**, 651
27. Vellinga, W. P., Ph.D. thesis, University of Groningen, 1996.
28. Vellinga, W. P. and de Hosson, J. T. M., *Mater. Sci. Forum*, 1996, **207–209**, 361.
29. Vellinga, W. P., de Hosson, J. T. M. and Vitek, V., *Acta mater.*, 1997, **45**, 1525.
30. Shashkov, D. A., Chan, D. K., Benedek, R. and Seidman, D. N., in *Interface Science and Materials Interconnection, Proceedings of JIMIS-8*. The Japan Institute of Metals, 1996, pp. 85–92.
31. Shashkov, D. A., Benedek, R. and Seidman, D. N., *J. Surf. Analysis (Japan)*, 1997, **3**, 377.
32. Benedek, R., Seidman, D. N. and Yang, L. H., *Microsc. Microanal.*, 1997, **3**, 333.
33. Benedek, R., Shashkov, D. A., Seidman, D. N., Muller, D. A., Silcox, J., Chisholm, M. F., Yang, L. H., in *Microscopic Simulation of Interfacial Phenomena in Solids and Liquids*, Vol. 492, ed. P. Bristowe, S. Phillpot, J. Smith and D. Stroud. Materials Research Society, Warrendale, PA, 1998, pp. 103–108; Benedek, R. *Phys. Rev. B*, in press
34. Chan, D. K., Ph.D. thesis, Northwestern University, 1994.
35. Li, D. X., Pirouz, P., Heuer, A. H., Yadavalli, S. and Flynn, C. P., *Acta metall.*, 1992, **40S**, 237.
36. Ernst, F., *Mater. Res. Soc. Symp. Proc.*, 1990, **183**, 49.
37. Mader, W., *Z. Metallk.*, 1989, **80**, 139.
38. Trampert, A., Ernst, F., Flynn, C. P., Fischmeister, H. F. and Rühle, M., *Acta metall.*, 1992, **40S**, 227.
39. Merkle, K. L., Buckett, M. I. and Gao, Y., *Acta metall.*, 1992, **40S**, 249.
40. Mayer, J., Gutekunst, G., Möbus, G., Dura, J., Flynn, C. P. and Rühle, M., *Acta metall.*, 1992, **40S**, 217.
41. Jang, H., Seidman, D. N. and Merkle, K. L., *Interface Sci.*, 1993, **1**, 61.
42. Jang, H., Seidman, D. N. and Merkle, K. L., *Mater. Sci. Forum*, 1993, **126–128**, 639.
43. Jang, H., Seidman, D. N. and Merkle, K. L., *Scripta metall. mater.*, 1992, **26**, 1493.
44. Benedek, R., Minkoff, M. and Yang, L. H., *Phys. Rev. B*, 1996, **54**, 7697.
45. Muller, D. A., Shashkov, D. A., Benedek, R., Yang, L. H., Silcox, J. and Seidman, D. N., *Phys. Rev. Lett.*, 1998, **80**, 4721.
46. Muller, D. A., Subramanian, S., Batson, P. E., Silcox, J. and Sass, S. L., *Acta mater.*, 1996, **44**, 1637.
47. Subramanian, S., Muller, D. A., Silcox, J. and Sass, S. L., *Acta mater.*, 1996, **44**, 1647.
48. Seidman, D. N., Krakauer, B. W. and Udler, D., *J. Phys. Chem. Solids*, 1994, **55**, 1035.
49. Rittner, J. D., Udler, D., Seidman, D. N. and Oh, Y., *Phys. Rev. Lett.*, 1995, **74**, 1115.
50. Udler, D. and Seidman, D. N., *J. Mater. Res.*, 1995, **10**, 1933.
51. Rittner, J. D., Udler, D. and Seidman, D. N., *Interface Sci.*, 1996, **4**, 65.
52. Rittner, J. D., Ph.D. thesis, Northwestern University, 1996.
53. Rittner, J. D. and Seidman, D. N., *Acta mater.*, 1997, **45**, 3191.
54. Udler, D. and Seidman, D. N., *Acta mater.*, 1998, **46**, 1221.
55. Udler, D. and Seidman, D. N., *Interface Sci.*, 1998, **6**, 259.
56. Krakauer, B. W. and Seidman, D. N., *Acta mater.*, 1998, **46**, 6145.